Modeling the 2012 Wharton basin earthquakes off-Sumatra: Complete lithospheric failure

Shengji Wei,[1,2] Don Helmberger,[1,2] and Jean-Philippe Avouac[1,2]

[1]   A sequence of large strike-slip earthquakes occurred west of Sunda Trench beneath the Wharton Basin. First reports indicate that the main shock was extremely complex, involving three to four subevents ($M_w > 8$) with a maze of aftershocks. We investigate slip models of the two largest earthquakes by joint inversion of regional and teleseismic waveform data. Using the $M_w 7.2$ foreshock, we developed hybrid Green's Functions for the regional stations to approximate the mixture of oceanic and continental paths. The main shock fault geometry is defined based on the back projection results, point-source mechanisms, aftershock distribution, and fine tune of grid searches. The fault system contains three faults, labeled F1 (89°/289° for dip/strike), F2 (74°/20°), and F3 (60°/310°). The inversion indicates that the main rupture consisted of a cascade of high-stress drop asperities (up to 30 MPa), extending as deep as 50 km. The rupture propagated smoothly from one fault to the next (F1, F2, and F3 in sequence) with rupture velocities of 2.0–2.5 km/s. The whole process lasted about 200 s, and the major moment release (>70%) took place on the N-S oriented F2. The $M_w 8.2$ aftershock happened about 2 h later on a N-S oriented fault with a relatively short duration (~60 s) and also ruptured as deep as 50 km. The slip distributions suggest that the earthquake sequence was part of a broad left-lateral shear zone between the Australian and Indian plates and ruptured the whole lithosphere. These earthquakes apparently reactivated existing fracture zones and were probably triggered by unclamping of the great Sumatran earthquake of 2004.

1.   Introduction

[2]   Earthquakes larger than $M_w 8.5$ are rare and generally occur on megathrusts along well-identified plate boundaries. The $M_w 9.2$ 2004 Sumatra-Andaman earthquake and the $M_w 8.6$ 2005 Nias-Simeulue earthquakes are two recent examples, with both located along the Indonesian subduction interface. The $M_w 8.6$ earthquake of 11 April 2012 occurred offshore of Sumatra in the Wharton Basin, not far from these two previous large events (Figure 1). This event was of quite a different nature: together with a $M_w 7.2$ foreshock 3 months before and a $M_w 8.2$ aftershock 2 h afterward, this earthquake formed part of a sequence of strike-slip events in an intraplate setting, rupturing a complex set of faults that intersected at high angles [*Meng et al.*, 2012] (Figure 1c). Good constraints on the sources of these earthquakes would help to clarify the underlying physics and to evaluate how different they

are from more standard large earthquakes along plate boundaries. Some insights have already been gained from back projecting the high-frequency (0.5–1 Hz) radiated seismic waves, from subevent point sources modeling of the teleseismic records, and from the aftershock distribution, revealing the complexity of the fault geometry, the rather deep centroid depth of the subevents, and the continuous rupture process [*Duputel et al.*, 2012; *Ishii et al.*, 2013; *Meng et al.*, 2012; *Satriano et al.*, 2012; *Yue et al.*, 2012].

[3]   However, some major issues remain yet to be addressed, such as: (1) the link between the sources of the high-frequency and very long period seismic waves, (2) the spatial-temporal pattern of the slip distribution at depth, and (3) the amount of associated stress drop. In this study, we address these problems based on finite-fault modeling of the two largest events in this earthquake sequence [e.g., *Ji et al.*, 2002a]. This technique provides information on the time evolution of slip during the seismic rupture based on the inversion of the seismic waveforms [e.g., *Ammon et al.*, 2005]. However, this kind of inversion is generally ill posed and therefore benefits from a priori constraints on the fault geometry and static slip distribution [e.g., *Konca et al.*, 2007; *Wei et al.*, 2011]. In an early attempt to model the source of the main shock, we were able to approximately fit the teleseismic records using a model consisting of a single planar fault striking N20°E (http://www.tectonics.caltech.
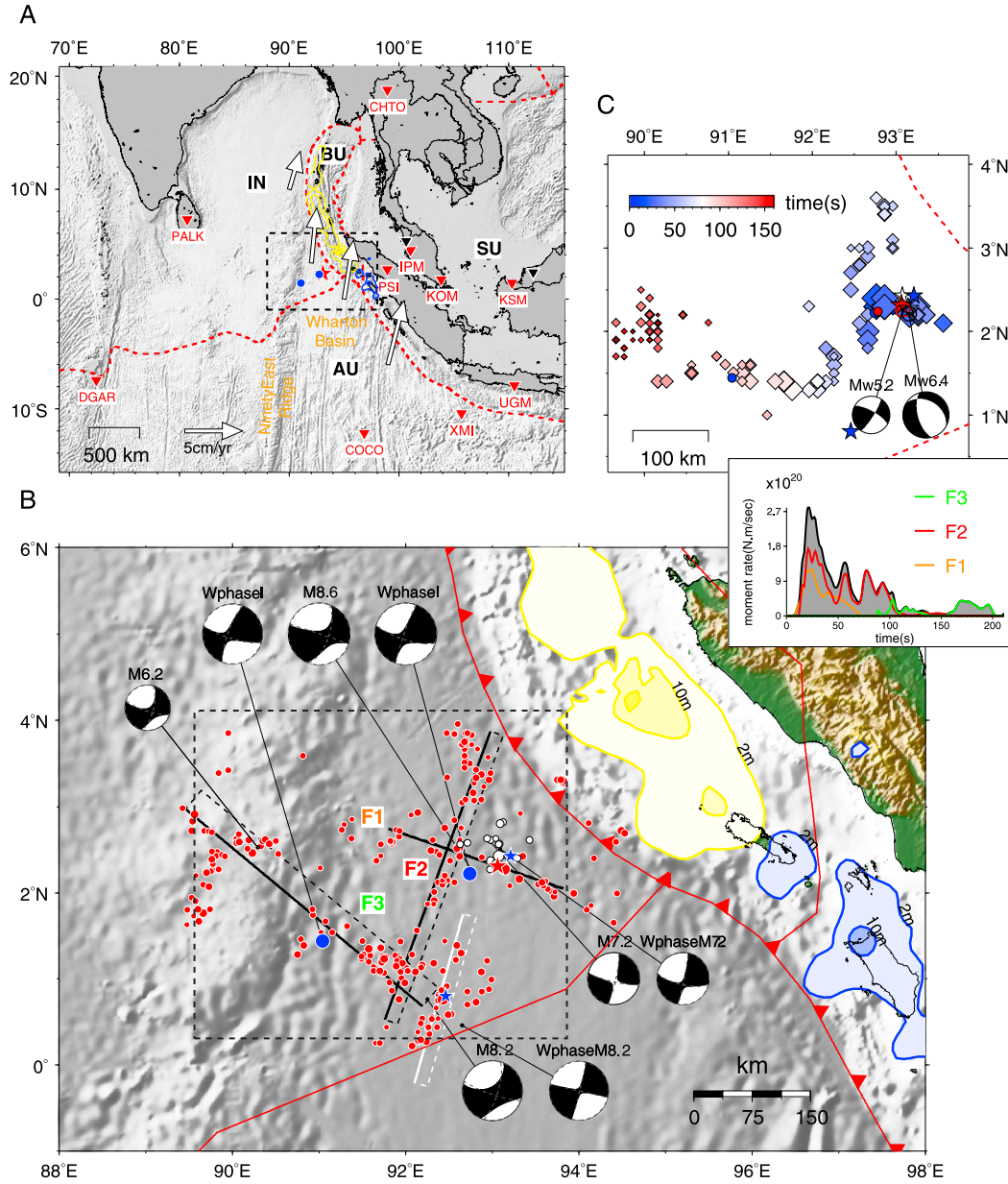

Figure 1. Tectonic setting and overview. (a) Tectonic setting in Sunda-Sumatra region. The arrows indicate the plate motion between the Australian Plate (AU), the Sunda Plate (SU), and the Indian Plate (IN). Red triangles are the regional stations used in the study. The main shock and the two black triangles are additional stations used for the $M_w8.2$ aftershock. The yellow and the blue contours show the slip model of the 2004 $M_w9.2$ and the 2005 $M_w8.6$ earthquakes, respectively. The red dashed lines are the plate boundaries defined by *Bird* [2003]. (b) Map view of the fault geometry consisting of three fault segments (F1, F2, and F3). The white rectangle is the map view of the fault segment used for inverting the $M_w8.2$ aftershock. The beach balls are the GCMT and W-phase solutions for the main shock, $M_w8.2$ aftershock, $M_w7.2$ foreshock, and the $M_w6.2$ aftershock. The blue and red stars indicate the NEIC epicenter of these events. The W-phase solution for the main shock includes two point source (blue dots), with moment magnitudes of 8.5 (I) and 8.3 (II). The red dots are the aftershocks in the first two months, and the white dots are the seismicity in the first 4 months before the main shock, locations are obtained from GFZ catalog. The yellow and blue contours are the same as in A. The inset shows the moment-rate function of the main event along with the contribution of each segment. (c) The beach balls display the mechanisms of the main shock, starting with the $M_w5.2$ event corresponding to the first 5 s and the $M_w6.4$ with the first 12 s. The back projection results are shown as diamonds [*Meng et al.*, 2012].
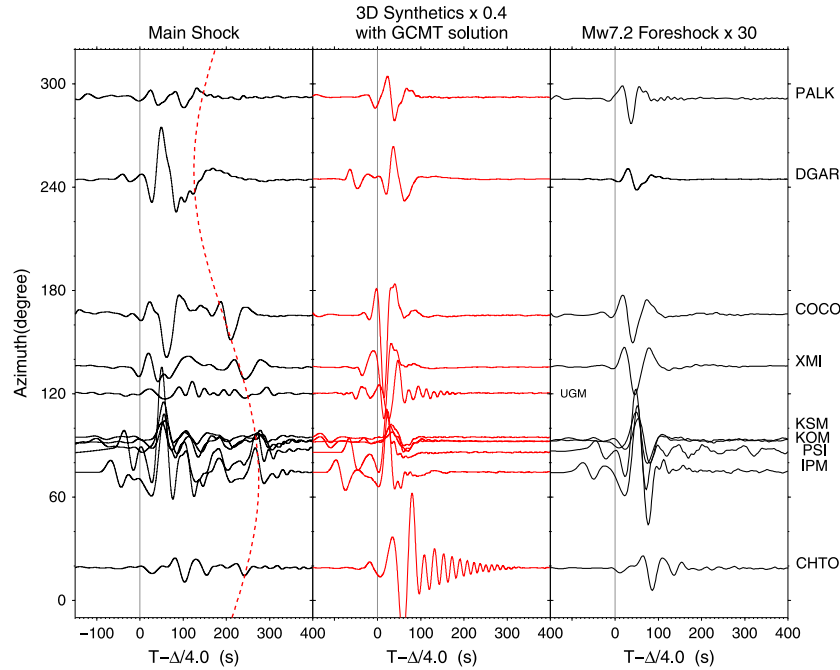
Figure 2. Regional vertical component for main shock and foreshock. Regional velocity record (vertical component) of the main shock (left) and foreshock (right), the SEM synthetics generated from a 3D model (red) of the main shock is shown in the middle. All the waveforms are filtered to 50 s and longer using a fourth-order 1 pass Butterworth filter. Note that the true amplitude is plotted with a different scaling factor for the 3D synthetics (0.4) relative to the foreshock (30). The red dashed line in the data is a prediction assuming a second point source located 300 km to the southwest (azimuth 250°) of the epicenter assuming that the seismic wave travels at a speed of 4.0 km/s.

edu/slip_history/2012_Sumatra/index.html). However, this simple model is inconsistent with the fault geometry suggested by the back projection results and the aftershocks. We also found it difficult to reconcile such a simple model with regional records. To obtain a more realistic source model, we used seismic waveforms recorded at both teleseismic and regional distances and assumed a more realistic fault geometry. The use of regional data is always challenging due to the sensitivity of these records to heterogeneities of the Earth structure. To overcome this difficulty, we calibrated regional paths using records of the $M_w7.2$ foreshock and the $M_w6.2$ aftershock.

[4] The remainder of the paper is organized as follows. First, we describe the methodology adopted. We then develop the hybrid Green's Functions for the regional seismic stations and test the resolution of the regional and teleseismic data, especially for resolving rupture depths. We then present the data set used and the modeling results obtained. In the final section, we discuss the seismotectonic implications of our findings.

2. Modeling Strategy

[5] To generate the kinematic slip models, we applied the method proposed by [*Ji et al.*, 2002a, 2002b], wherein a finite-fault model is used containing a distribution of subpatches (small rectangles) that can slip with various slip amplitudes, rakes, rise times, and delays in rupture onset (rupture velocity). The synthetics generated from such a model are compared with observed waveforms in the

"wavelet" domain, and an optimized slip model is produced using a simulated annealing algorithm in which a large number of possible slip models are tested.

[6] One of the advantages of this method is its ability to handle multiple data sets, which can be recorded at locations very close to the fault or at teleseismic distances. To conduct inversions on these waveform data, we must assume a 1D velocity model to generate the Green's Functions. At teleseismic distances, we use *P* (vertical) and SH waves in the inversion where the crustal structure can be distinct beneath the source and receiver location. The Green's Functions are generated by a combination of the reflection and refraction coefficient method (source region) and the ray theory (mantle region). Since the takeoff angles for teleseismic stations are quite small, the ray path is almost straight down from the source and thus much less sensitive to any lateral variations in the 3D structure. Thus, teleseismic body waves can provide constraints on the rupture detail of large earthquakes, in particular the depth of rupture, because the depth phases (pP and sP) are especially clear as a result of the relatively simple oceanic structure in the source region.

[7] In contrast, the regional records are dominated by surface waves in the frequency band of interest. In Figure 2, we present the vertical components of the regional waveforms for both the main shock and the $M_w7.2$ foreshock. (See Figure 1 and Table 1 for the location of the foreshock.) The velocity waveforms were filtered to 50 s and longer, to reduce the influence of the finite rupture process of the $M_w7.2$ foreshock. At this frequency band, the foreshock can be considered as a point source, and we observe very

Table 1. Source Parameters of the Four Largest Events in This Earthquake Sequence (2012-01-01–2013-01-10)

		Origin Time	Location (lat°,lon°)	Depth	Mechanism (strike°/dip°/rake°/Mw)
M7.2	GFZ	2012-01-10 18:36:58.00	2.43, 93.07	10.0	189(284)/66(79)/−11(−154)/7.1
	NEIC	2012-01-10 18:36:59.08	2.43, 93.21	19.0	NAN
	GCMT	2012-01-10 18:37:13.3	2.59, 92.98	23.7	12(103)/83(81)/−9(−173)/7.2
	This Study	Same as NEIC	Same as NEIC	16.0	10(103)/86(57)/−33(−175)/7.23
M8.6	GFZ	2012-04-11 08:38:35.00	2.27, 93.14	16.0	109(199)/77(90)/180(13)/8.6
	NEIC	2012-04-11 08:38:36.72	2.33, 93.06	20.0	NAN
	GCMT	2012-04-11 08:38:36.70	2.35, 92.82	45.6	20(76)/76(85)/5(166)/8.6
	This Study	Same as NEIC	Same as NEIC	24.0	
M8.2	GFZ	2012-04-11 10:43:09.00	0.76, 92.43	30.0	17(107)/87(89)/0(−176)/8.2
	NEIC	2012-04-11 10:43:10.85	0.80, 92.46	25.0	NAN
	GCMT	2012-04-11 10:43:38.24	0.90, 92.31	54.7	17(107)/87(83)/−7(−177)/8.2
	This Study	Same as NEIC	Same as NEIC	25.0	
M6.2	GFZ	2012-04-15 05:57:36	2.46, 90.23	10	15(107)/71(84)/−5(−160)/6.2
	NEIC	2012-04-15 05:57:40.06	2.58, 90.27	25.0	NAN
	GCMT	2012-04-15 05:57:42.57	2.49, 90.31	33.0	13(108)/68(78)/−13(−158)/6.3
	This Study	Same as NEIC	Regional-CAP	46.0	7(98)/68(88)/−2(−158)/6.21
			Tele-CAP	40.0	13(105)/77(80)/−10(−167)/6.26

simple waveforms on various azimuths. The records from the main shock display a strong azimuthal pattern, indicating a much longer duration and more complicated rupture process than for the foreshock. Thus, including these data in the finite-fault inversion helps to improve the resolution in the absence of geodetic data. As shown in Figure 2, the records are mainly dominated by Rayleigh waves. The group velocity of these Rayleigh waves is about 4.0 km/s at this frequency band, which is much slower than the apparent *P* wave velocity (~20 km/s) at teleseismic distances. The slower-moving surface waves provide key information about the timing and location of major asperities.

[8] We must also assume a 1D velocity model to compute Green's Functions for regional waveform inversion. However, a single 1D velocity model may not be sufficient in this case, considering the mixture of oceanic and continental paths (Figure 1A). For stations XMI, COCO, DGAR, and PALK, the paths are almost oceanic, but the paths for other stations are a mixture of both oceanic and continental. Using the $M_w7.2$ foreshock as a calibration event, we developed hybrid Green's Functions for the regional paths, which are presented in the next section along with the study of the depth resolution for the regional and teleseismic data.

3. Regional Path Calibration and Depth Resolution of Regional and Teleseismic Data

[9] Because the propagation of the regional wavefield involves oceanic and continental paths, it is essential to choose appropriate 1D velocity models to approximate the real 3D structure. For this study, we used the $M_w7.2$ foreshock as a calibration event and adopted the GCMT (http://www.globalcmt.org/) solution to calculate the 1D synthetics. We tested two 1D velocity models according to the path characteristics and labeled these ref2 and ref3. Ref2 is the PREM model, and ref3 is similar to ref2, but with the crust replaced by the oceanic crust extracted from Crust2.0 [*Bassin et al.*, 2000] in the source region—see Figure 3A for more detail of the models. The Green's Functions were computed using a frequency-wave number integration method [*Zhu and Rivera*, 2002] and convolved with a 25 s triangle source time function to generate synthetics. We then compared these waveforms with the data; two representative stations are

shown in Figure 3B. To better understand the effect of the 3D structure, we also downloaded 3D synthetics calculated using the Spectrum Element Method (SEM) from http://global.shakemovie.princeton.edu/ [*Tromp et al.*, 2010] for comparison. The same GCMT solution is assumed in these 3D synthetics, and the 3D velocity model is composed of the mantle model S36ANI [*Kustowski et al.*, 2008] and the model Crust2.0 [*Bassin et al.*, 2000]. We filtered all the waveforms to 50 s and longer to suppress the effect of the finite rupture process. As shown in Figure 3B, the 1D synthetics are not that sensitive in terms of the vertical and radial components. However, the tangential component does show a difference, with the oceanic path (COCO) better modeled by the oceanic crust (ref3) and a mixed path (KOM) more consistent with the average model (ref2). This sensitivity can be seen better in the cross-correlation coefficients (CCs) between the data and various synthetics (Figure 3C). Note that the fits of the 1D synthetics are no worse than those of the 3D synthetics. The waveform comparisons for all the stations are given in Figure S1. The tangential CCs in Figure 3C indicate that the stations can be divided into two groups according to their path characteristics, where the oceanic paths of XMI, COCO, DGAR, and PALK can be approximated by ref3 while the mixed paths of CHTO, IPM, PSI, KSM, and KOM are more consistent with ref2. These two models were used for the corresponding stations during the finite-fault inversion of the main shock, for the $M_w8.2$ aftershock, and for testing purposes.

[10] We also conducted a few more tests on the resolution of the regional data by searching for the best point source mechanism for the $M_w7.2$ foreshock, assuming the hybrid Green's Functions. This was achieved following a grid-search procedure where all possible mechanisms and depths were tested and the synthetics were allowed to shift for maximum alignment, referred to as the Cut-And-Paste (CAP) method [*Wei et al.*, 2012; *Zhao and Helmberger*, 1994; *Zhu and Helmberger*, 1996]. While most inversions assume their Earth model to be correct and map differences in Green's Functions from the real Earth into nondouble couples, the CAP method allows timing shifts and performs a grid search for the best double-couple source. We rotated the data to vertical, radial, and tangential components, assuming the NEIC epicenter location (2.43°N, 93.21°E), then searched for the
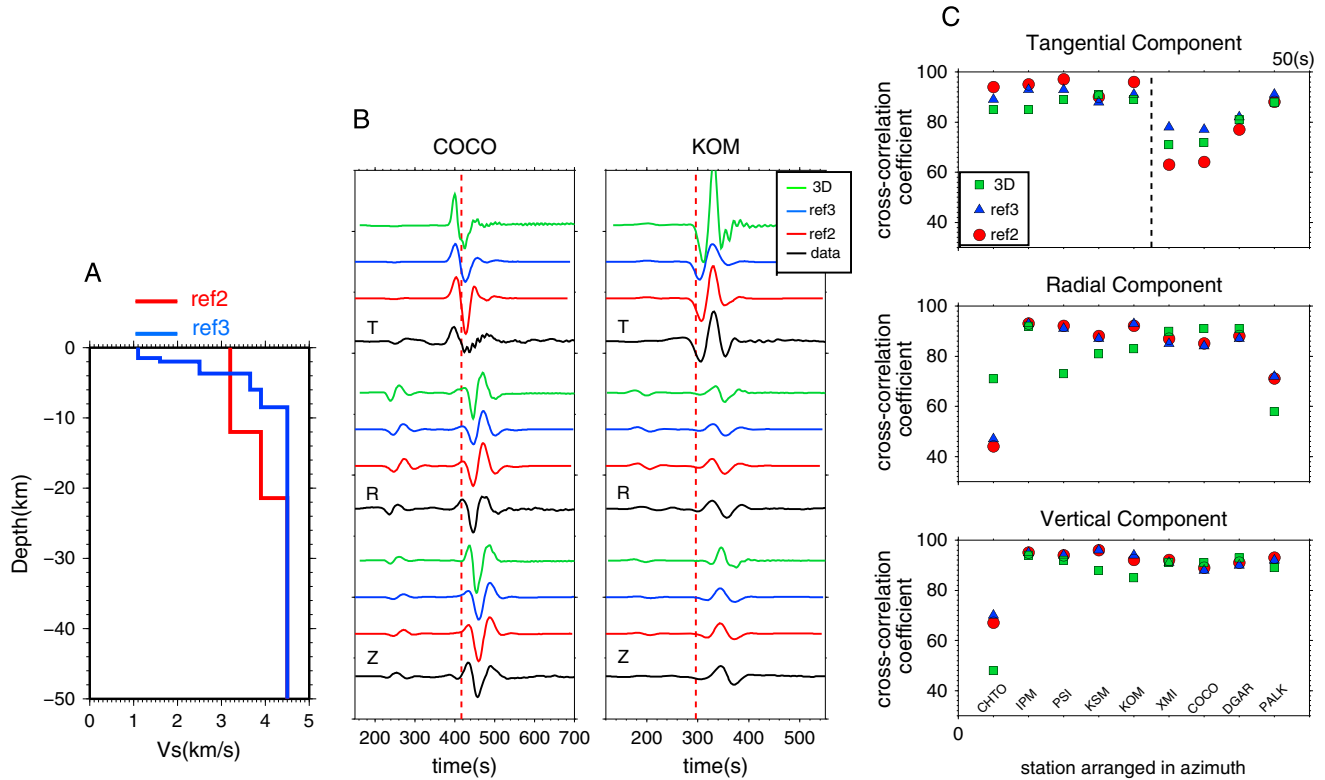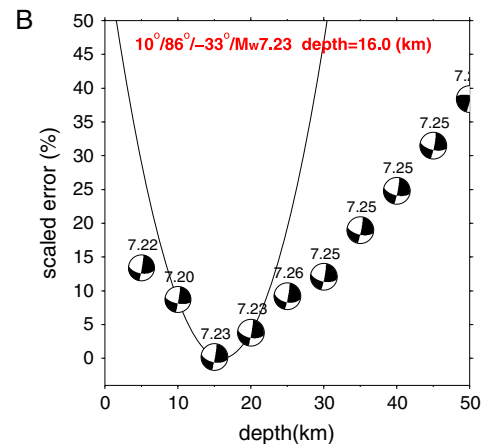
Figure 3. 1D velocity models and path examples. (a) Two 1D velocity models used in generating the regional Green's Function. (b) Three component waveforms at two representative stations. The 1D synthetics (ref2 in red, ref3 in blue), 3D synthetics (green) and data (black) are filtered to 50 s and longer. (c) Summary of waveform cross-correlation coefficients (CCs) between data and various synthetics. Note that model ref3 can fit the oceanic paths better while the mixed paths favor model ref2, as separated by the dashed line.

best strike, dip, rake, and depth in the ranges of $0 – 360°$, $0 – 90°$, $−180 – 180°$, and $5 – 50\,km$, with intervals of $2°$, $2°$, $2°$, and $5\,km$, respectively. The double-couple mechanism that we obtained at the best depth ($15\,km$) was $10°/86°/−33°/7.23$ for strike/dip/rake/M_w. The corresponding waveform fits and depth resolution are shown in Figure 4. Note the high CCs for most of the components. The mechanism is in good agreement with the GCMT double-couple solution ($12°/83°/−9°/7.2/22\,km$)—see Table 1 for more details. Here we emphasize the good resolution of the centroid depth obtained from the inversion of regional data.

[11] Because we used both regional and teleseismic data in the finite-fault inversion of the main shock, we also wished to test the resolution of the teleseismic data, particularly the depth resolution. We therefore conducted a similar test for both the teleseismic and regional data for an $M_w6.2$ aftershock. This event is located on the western end of fault segment F3 (Figure 1). The reason for choosing a smaller aftershock, rather than the $M_w7.2$ foreshock, is because the latter is too complicated to be considered as a point source at the frequency band of interest for teleseismic modeling. We downloaded data for 32 teleseismic P waves from IRIS and converted them into velocities. Then we ran the tele-CAP inversion scheme (similar to CAP but using teleseismic data) on the vertical components (P waves) to grid search for the best point source mechanism. The strike, dip, rake, and depth

were searched in the ranges $0 – 360°$, $0 – 90°$, $−180 – 180°$, and $5 – 65\,km$, with intervals of $2°$, $2°$, $2°$, and $2\,km$, respectively. The double-couple mechanism we obtained at the best depth ($46\,km$) was $7°/68°/−2°/6.21$ for strike/dip/rake/M_w, assuming model ref3 in the source region. This mechanism is again in good agreement with the GCMT solution ($13°/68°/−13°/6.3$); see Table 1 for more details. Note the fairly deep centroid depth ($46\,km$) of this aftershock. The depth resolution of the inversion is shown in Figure 5A, with the waveform fitting all the stations given in Figure S2. The sharp convergence of error vs. depth indicates that the depth of this event was resolved rather well. This can be better seen in a detailed analysis for station BBOO (Figure 5B), in which the data are plotted against the synthetics generated at different depths. As shown, the differential times between direct P wave and depth phases (pP and sP) provide key constraints on the depth. Together with the relative amplitude ratios between various phases and the azimuthal samplings of the radiation pattern, the teleseismic data allow us to pin down the earthquake mechanism quite precisely. In addition, we applied the same CAP method as for the foreshock on the regional data to invert for the point source solution. The mechanism obtained at the best depth ($40\,km$) was $13°/77°/−10°/6.26$ (strike/dip/rake/M_w), which is remarkably consistent with the teleseismic mechanism and the GCMT solution (Table 1). The inversion results are shown

Figure 4. CAP inversion result of the foreshock. (a) The Cut-And-Paste (CAP) inversion result for the foreshock. The waveform fits for the best depth (15 km) are shown. The station names are indicated at the beginning of the record along with distance in km (upper) and azimuth in degree (lower). The first number below each waveform pair is time shift needed to aligned synthetic and data, and the second number is waveform cross-correlation coefficient in percentage. A positive time shift indicates the velocity model is too fast. The red beach ball at the top shows the lower hemisphere projection of the mechanism ($10°/86°/−33°/7.23$ for strike/dip/rake/M_w), and the dots indicate station projections on the lower hemisphere, each according to its first arrival P wave takeoff angle. (b) Depth resolution of the inversion.

in Figure S3. The depth resolution is provided by the combination of Pnl waves and surface waves. As indicated in Figure S4, Pnl and Love waves are less dependent on depth than Rayleigh waves, so the relative amplitude ratio between the various components provides a good constraint on the source depth. Note that the teleseismic depth (46 km) includes 4 km of water on top of the velocity model, while the regional inversion does not include the water layer. Thus, the regional depth (40 km) is also in good agreement with the teleseismic results. The uniform inversion results between the two data sets indicate the self-consistency of the model set-up, thereby allowing for joint inversion of the detail rupture process for large events. Moreover, the timing shifts required to align the data and the synthetics are in general agreement between the foreshock and the aftershock, i.e., the time shifts for Love waves. If we use the time shifts of one event to relocate the other using the method of [*Wei et al.*, 2012], they move less than 15 km, which is smaller than the size of our horizontal grid (20 km) for the finite-fault inversion.

[12] Using the M_w7.2 foreshock and the M_w6.2 aftershock, we obtained the regional path calibrations and

demonstrated that the resolution of both the regional and the teleseismic data constrained the earthquake mechanism, especially in terms of depth. We then used the regional surface waves and teleseismic body waves to invert the finite rupture process of the main shock, as discussed in the following sections.

4. Data Preparation and Inversion Setup

[13] For large earthquakes of the type discussed herein, teleseismic (30 – 90°) P and SH waves are usually well recorded. Stations in this distance range are free from the interference of upper mantle triplication and thus are extensively used for finite-fault inversion. We downloaded the broadband teleseismic data from IRIS (http://www.iris.edu/hq/). Instrument responses were removed from the data and converted into displacements. P waves were low-pass filtered to 1 s and SH waves were low-pass filtered to 2 s. Because there were many records to choose from, we picked stations based on their relative waveform quality and their agreement with neighboring stations. We selected 31 P wave and 24 SH wave components, providing good azimuthal coverage of the
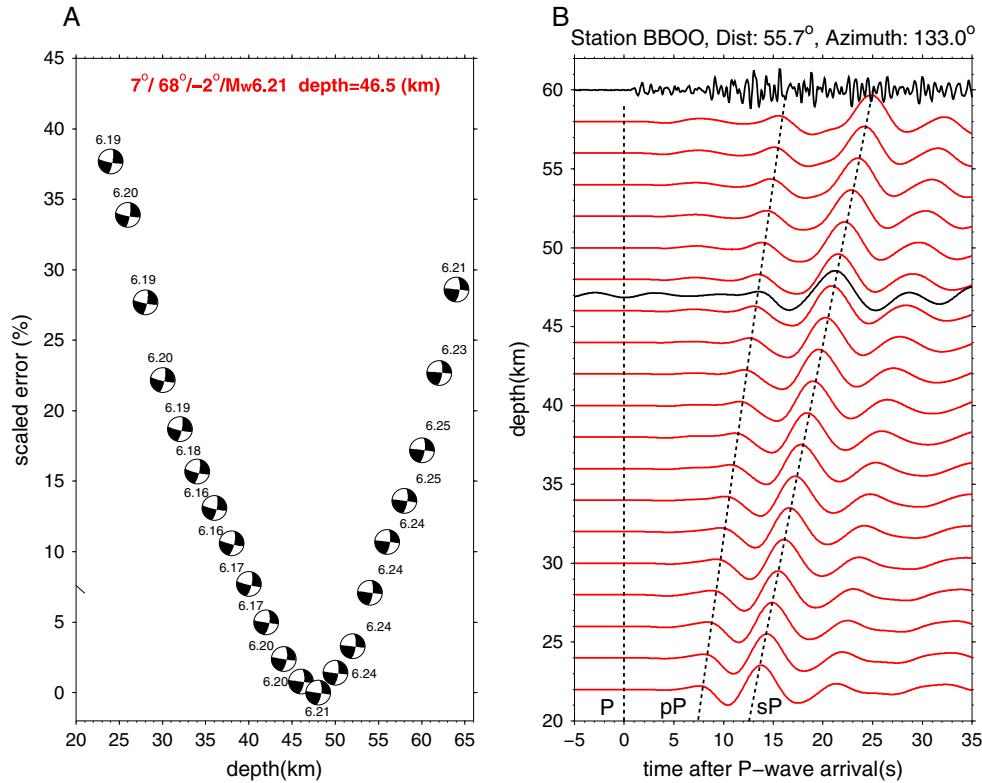
Figure 5. Teleseismic inversion of M$_w$6.2 aftershock (a) Display of the depth resolution of teleseismic *P* wave inversion (tele-CAP) for the M$_w$6.2 aftershock. (b) The synthetics (red) generated at different depths are plotted with the data (black) for station BBOO. Both the data and synthetics are filtered to 6 s and longer as used in the inversion. The high-pass filtered (>1 Hz) data are plotted on the top to show the high-frequency first arrival of direct *P* wave. The depth phases (pP and sP) are indicated by the dashed lines.

radiation pattern as shown in Figure 6, in which the size of the triangle is proportional to the maximum amplitude of the data. Note the large *P* wave amplitude at GNI and ABPO relative to strong SH waves at TLY and PAF: this type of 45° rotation of peak amplitude direction between *P* and SH waves is consistent with a typical strike-slip mechanism. Since we intended to use the direct *P* and SH waveforms to constrain the rupture process, we did not include later arrivals, such as PP and SS phases, in the time window for the inversion. Using the PP phase as an example, the differential arrival time between the PP and P phases increases from about 70 s to 220 s as the epicentral distance increases from 30° to 90°. The duration of the main shock is about 150 s, according to the back projection results [*Meng et al.*, 2012]. Thus, using stations beyond 50° avoids these phases and provides a long enough time window to constrain the rupture.

[14] In comparison with the teleseismic *P* waves, the regional data do not suffer from the problem of the later phases, as demonstrated in Figure 2. The records of the M$_w$7.2 foreshock show clear and simple pulses when filtered to 50 s and longer, and no later arrivals in the time window of interest. These regional waveforms are mainly dominated by surface waves, and the apparent travel speed is about 4.0 km/s, much less than that of teleseismic body waves. This implies that the regional surface wave is more sensitive to the horizontal location of the asperities whence the excitation originated. Regional surface waves can provide a good constraint for the rupture in the horizontal direction, complementary to

teleseismic body waves, which correspond to a small takeoff angle in the source region and are more sensitive to the rupture in terms of depth (the vertical direction).

[15] The regional data were downloaded from IRIS and were converted to velocities after removing the instrument responses. *P* wave first arrivals were handpicked, and a time window of 800 s was used for inversion. Because the waveform is fairly simple, as shown by the M$_w$7.2 foreshock (Figure 2), the complexities in the waveform record of the main shock are mainly due to the finite rupture process. These regional data provide key constraints for resolving the major rupture asperities.

[16] During the inversion, we divided the rectangular fault segment into smaller subfaults with dimensions of 20 km along the strike and 5 km along the dip. We searched for the slip from 0 to 40 m at 1 m intervals, with the cosine shape rise time chosen to range from 3 to 24 s at intervals of 3 s, and the rupture velocity varying from 1.8 to 2.8 km/s at intervals of 0.1 km/s. A Laplacian smoothing algorithm is applied to minimize the difference between the slip on adjacent subfaults. The misfit function is defined in the wavelet domain and a combination of L1 and L2 norm is used, as defined in equation (11) in [*Ji et al.*, 2002a]. During the joint inversion, the regional and teleseismic data sets are equally weighted which is achieved by normalizing the misfit error of each data set by the minimum errors obtained in inverting individual data set. Within each data set, the weight used for each seismogram was the same. The regional data were fitted
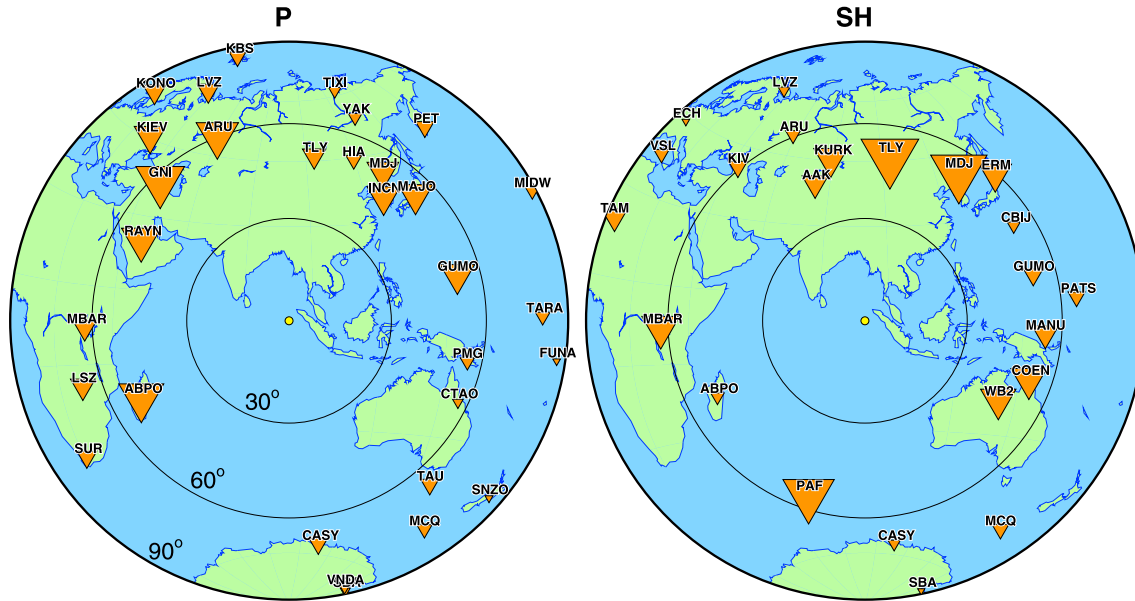
Figure 6. Teleseismic station map. The station distribution of teleseismic *P* and SH components used in the inversions where the size of triangle is proportional to the maximum displacement amplitude for each station. Note that the largest amplitude directions between the *P* and SH waves are rotated by 45° as predicted for a strike-slip event.

in the frequency band of 50 s and longer. Because the earthquake occurred in the ocean and the multiple water bounds can generate a good size signal for the teleseismic *P* waves [*Chu et al.*, 2011], we incorporated a 4 km water layer on top of the velocity model in the source region when we computed the teleseismic Green's Functions.

[17] Due to the lack of near fault geodetic and strong motion data, such a finite-fault inversion is ill posed and suffers from the nonuniqueness of the solution. Thus, we conducted several checkerboard tests to better understand the resolution of the data sets we have. As shown in Figure S5, we generate the synthetic data using checkerboard-like slip distributions with asperity dimension of 60 km × 15 km (A) and 100 km × 20 km (B), respectively. We then inverted the synthetic data using the inversion setup as described previously. The corresponding results are presented in (C) and (D) where the larger asperities are much better resolved than the smaller ones which gives us the confidence on the resolution of asperities with dimension greater than 100 km × 20 km. We also conduct a test to find out the appropriate smoothing factor for the joint inversion. As indicated in Figure S6, we choose the smoothing factor than can dramatically reduce the misfit but not too small to lose the control of the inversion to generate major asperities. The smoothing process can also be seen in the other supplement materials (Anim. S1 and Anim. S2).

5. Inversion Results

[18] In this section, we present the details of the fault geometry and the timings between different faults, along with an analysis of the associated slip models. Then inversions using teleseismic data only and regional data only are compared with the joint inversion model to show the sensitivity of the different data sets. Further decomposition of the finite

rupture process on fault F2 is presented at the end of this section to show the details of the waveform inversion.

5.1. Fault Geometry and Relative Timings

[19] The results from back projection reveal that the rupture initiated from the WNW-ESE oriented fault, then propagated to the NNE-SSW oriented fault. The strikes of these two faults are consistent with the GCMT mechanism as well as the W-phase mechanism [*Duputel et al.*, 2012]. The distribution of aftershocks also delineates these two faults near the epicenter (Figure 1). Note that the aftershock locations plotted in Figure 1 were obtained from the catalog maintained by GFZ (http://geofon.gfz-potsdam.de/eqinfo/special/gfz2012hdex/), which has more stations in this region than the global network does. Thus, we used the two conjugate fault planes in the GCMT best double-couple solution to approximate the rupture, and we assumed the rupture started from the fault plane with a strike of 289° (F1), since the epicenter lies to the east of the intersection point of the two fault planes. The epicentral location was adopted from the NEIC (2.311°N, 93.063°E) catalog, with a depth of 24 km. A third fault plane (F3) was added to the southern end of fault F2, to account for the late WNW-ward rupture as indicated in the regional surface waves, which is also supported by the back projection results and the distribution of the aftershocks. The strike of F3 (310°) was chosen to follow the back projection rupture trace and the linearized aftershock distribution. The dip angles for F1 and F2 were first set to the number in the GCMT solution, which were 89° and 64° for F1 and F2, respectively. Based on these initial values, we applied a perturbation of 20° to the dip angle at intervals of 5°, to fine tune these values. We found that the inversion fitted the teleseismic data slightly better with a dip angle of 74° for F2, and we used this value in the following inversions. The dip angle of F3 was determined using a trial-
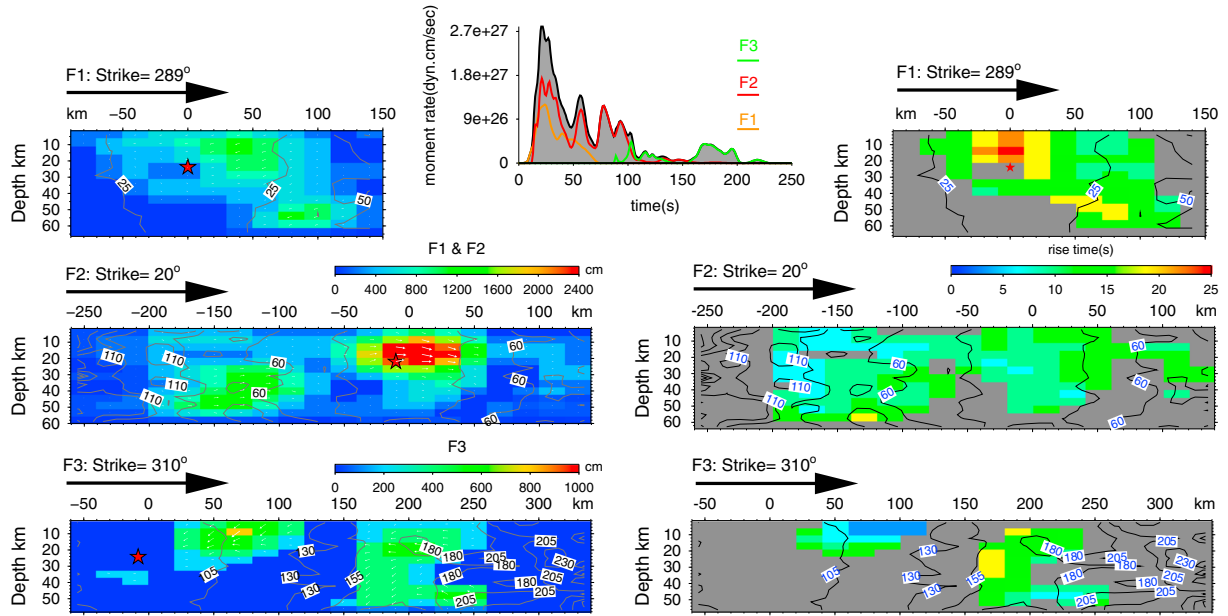
Figure 7. Slip model, moment-rate function, and rise time. The depth profiles of slip distribution (left), rise time (right), and moment rate (middle) of the joint inversion finite-fault model are presented with slip and rise times color coded. The contour lines are the rupture starting times relative to the epicenter origin time with the interval of contours set at 25 s. The white arrows in slip distribution indicate the rake angle per element. The contribution from the various fault segments is shown in the moment rate function with the gray-shaded region indicating the total radiation rate. Note that after 60 s, only individual fault segments are radiating significant energy, that is F2 from 60 s to 100 s and F3 thereafter.

and-error procedure, since there is no moment tensor solution of this portion of the rupture, due to the relatively weak signals. In fact, the regional surface wave records have shown some evidence for a different mechanism for this rupture. As shown in Figure 2, the Rayleigh wave amplitude ratios between the early rupture and the late rupture change dramatically at different azimuths, such as for stations XMI and IPM. We cannot therefore simply adopt the dip angle of F1 or F2 for F3. The grid search revealed that a dip angle of 60° is most appropriate for F3 in terms of fitting the relative amplitude of the regional surface waves. The problem could also be solved by breaking F3 into two segments, but this would introduce even more parameters.

[20] Finite-fault inversion aims to resolve the spatial-temporal distribution of the rupture. However, this process becomes more complicated when multiple faults are involved. As discussed previously, we determined the fault geometry by fitting the regional data and applying other constraints such as back projection and the distribution of aftershocks. In addition, we also needed to determine the relative timing of the rupture between different faults. Because the three faults are connected, we assumed the intersection point was where the rupture started on the new fault. Thus, we have two more rupture initiations on F2 and F3, shown as red stars in Figure 7. Because the rupture propagated first from F1 to F2 and the rupture on these two faults produced the strongest signals in both the teleseismic and the regional records, we focused primarily on the timing of the rupture between these two faults. A time delay was assumed between the rupture on F1 and F2, and a grid search, with an interval of 2.5 s, was applied to find the best value. A delay of 10 s was the most appropriate, especially for fitting

the teleseismic P waves. Similarly, we determined the delay of the rupture between F3 and F1 to be about 80 s.

[21] Our best combined slip distributions and rise time plots are shown in Figure 7. The result of each iteration in the simulated annealing inversion process is shown in Anim. S1 (see supplement), where the convergence of the inversion can be seen. The final result indicates that the total duration of the earthquake was about 200 s and the total moment was 1.3×10^{22} N·m. This moment is about 40% larger than the best double-couple moment of the GCMT solution (8.96×10^{21} N·m). The discrepancy is mostly due to the fact that the GCMT is a point source solution, the moment constraint mainly a result of fitting the strongest asperity of the source. When the source duration is close to or longer than the period used to determine the GCMT solution, the moment contributed by late rupture is likely to be missed. Similarly, for the 2004 Sumatran-Andaman M_w9.2 Earthquake, the GCMT solution yielded an M_w of 9.0. The total moment given by the two-point-source approximation for this event was 1.15×10^{22} N·m [*Duputel et al.*, 2012], which is consistent with the moment we obtain here. As shown in the joint inversion slip model (Figure 7), the earthquake ruptured the two conjugated fault planes almost simultaneously, and the slip reached a maximum of about 25 m on F2, corresponding to the rupture between 15 and 40 s. Over 70% of the moment release occurred within the first 50 s of rupture. Note that the late rupture on F2 at around 75 s is as deep as 50 km. The rupture on F3 involved two separate asperities (around 110 and 200 s after rupture initiation on F1). This part of the rupture is required to fit the late arrivals in the regional records, as discussed earlier. The moment of the rupture on F3 is 1.96×10^{21} N·m ($\sim M_w$8.1). Rise times are
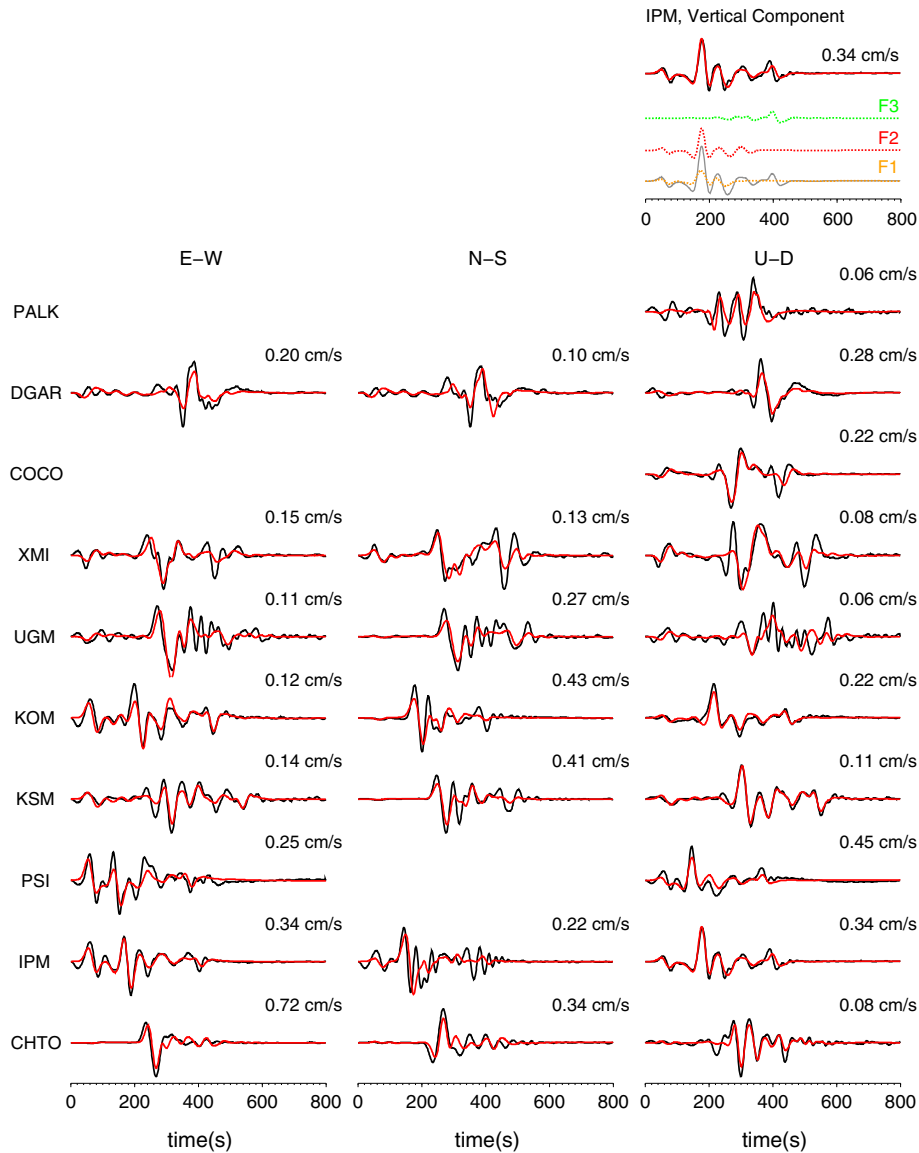
Figure 8. Regional waveform fits for the joint inversion model. The three component regional waveform fits for the joint inversion model are shown with data in black and synthetic in red. All the waveforms are filtered to 50 s and longer. Station names are indicated at the beginning, and the number above each trace indicates the maximum amplitude of the data with the synthetics on the same scale. The empty spaces are clipped components. One example component at the top (IPM) displays the decomposition of the synthetics into the contributions from each fault segment.

estimated to be about 20 s during the initial phase of the rupture on F1 and around 10 s for the rest of the rupture. Detailed waveform fitting analysis to demonstrate the sensitivity of the different data sets is discussed in section 5.3.

5.2. Regional Waveform Fits

[22] The regional waveform fits for the best joint model are shown in Figure 8, with an example showing the contribution of each fault segment at station IPM (top right). The decomposition of the synthetics for all the components is given in Figure S7. As shown, the strongest signals in the data are mainly from F1 and F2, corresponding to the rupture of the first 50 s (moment-rate function in Figure 7). The rupture on the two conjugated faults has the largest slip amplitude, which is about 25 m on F2 near the intersection of F1 and

F2. This location is in agreement with the coordinates of the point source mechanism of the GCMT solution and the first source of the W-phase solutions (Figure 1B). There was some rupture following on at the southern end of F2, which took place at around 50–100 s . This portion of the rupture explains the signals in the data after the strongest pulses (Figure 8 and Figure S7). The last rupture occurred on F3, almost unilaterally toward the west along the strike. Decomposition of the synthetics indicates that the late arrivals on the eastward stations (PSI, IPM, KOM, KSM, and XMI) mainly came from the asperities on this fault. The rupture on F3 is about 250 km to the west of the major asperity on F2, which corresponds to a travel time of ~60 s for the Rayleigh wave at the 50 s frequency, making the tails of the eastward records much longer. Conversely, the
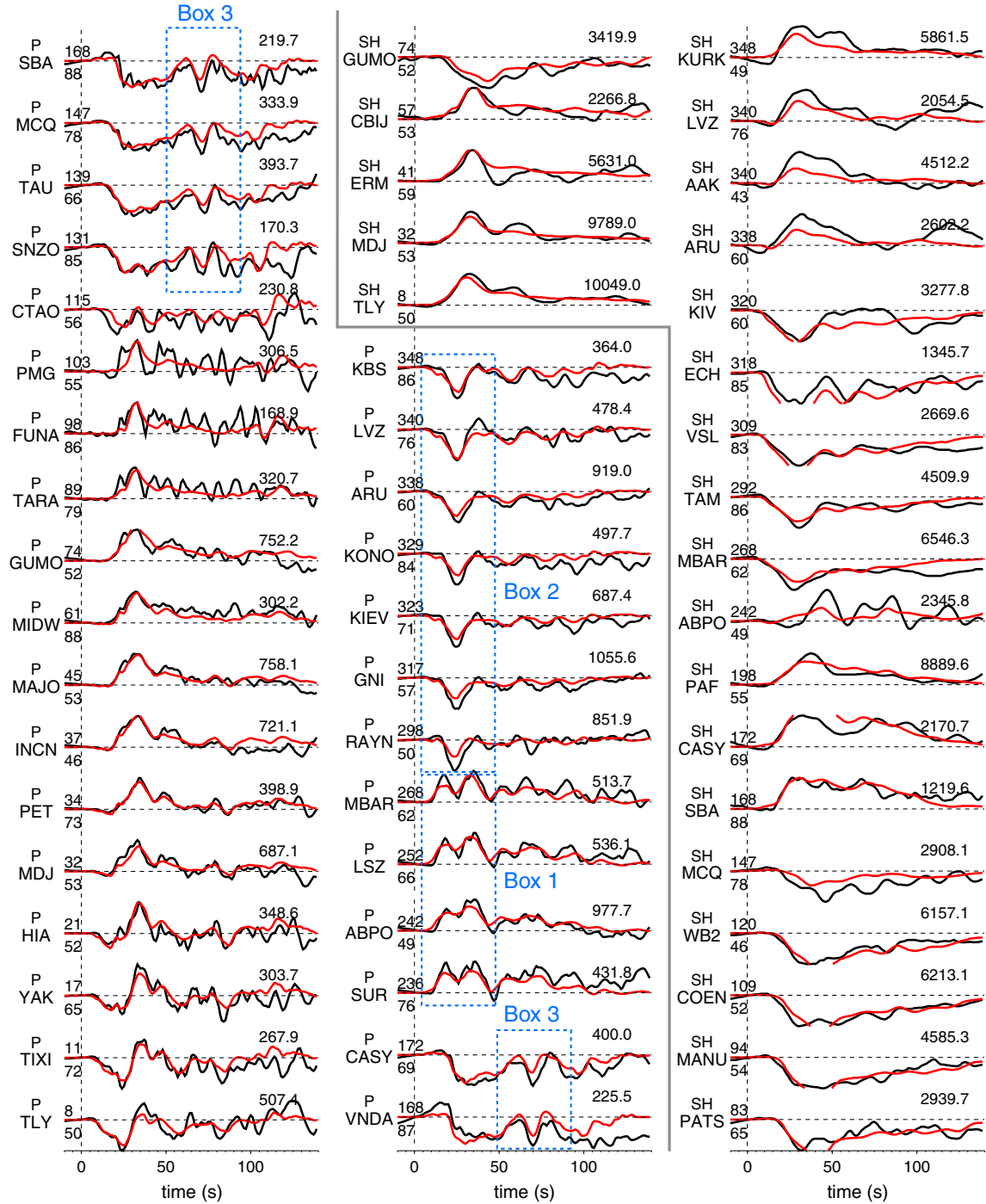
Figure 9. Teleseismic waveform fits. The teleseismic waveform fits for the joint inversion model are presented where *P* and SH waves are separated by the heavy gray line. The data are displayed in black and synthetics in red; the station name is indicated at the beginning of each trace with epicenter distance in degree (lower) and azimuth (upper). The maximum amplitudes of data in micrometers are shown at the end of the seismograms. Stations at three azimuths groups are indicated by the dashed rectangles (Box1, Box2, and Box3) with representative stations shown in Figure 10.

westward stations (DGAR, PALK, and COCO) recorded more compact waveforms, which is explained by the directivity of the rupture and the difference in the locations of the asperities. Some paths running along the trench are particularly complex (UGM and XMI) and more difficult to model using a 1D velocity model.

[23] We realize that most of the rapid changes in slip are not controlled by these long period (>50 s) regional data, because inversions of these recordings without teleseismic data show more gentle changes (Figure S8). For comparison, we include a model generated by inverting the teleseismic data alone. The slip model from the regional data only inversion
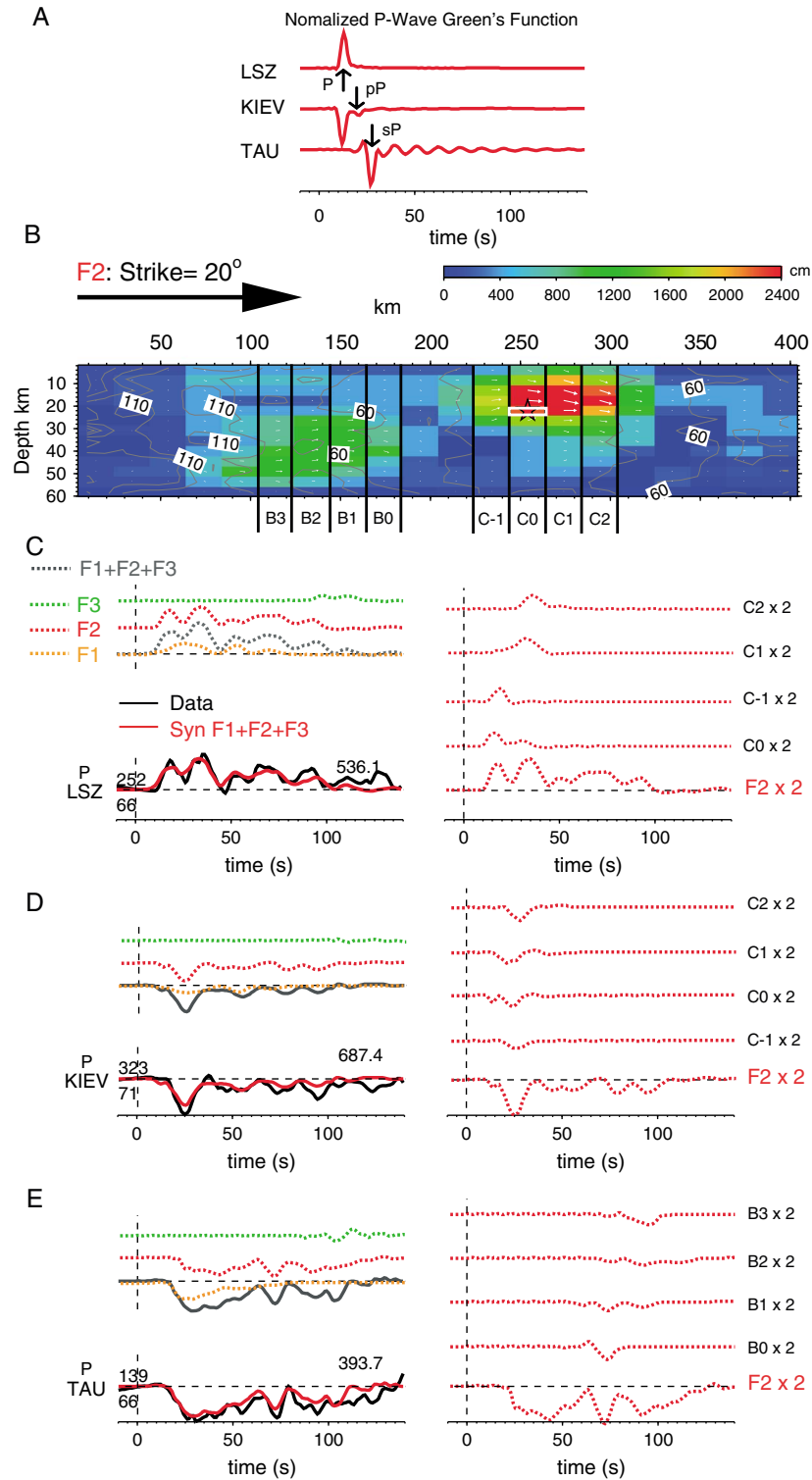
Figure 10. Representative teleseismic fits for stations at azimuth of 250°, 320°, and 140°. We selected three representative teleseismic stations (LSZ, KIEV, and TAU) from three groups of stations (Boxes) as indicated in Figure 9 for detailed modeling. An example of normalized Green's Functions for the three stations, direct P, and ocean bottom reflection pP and sP phases are indicated by arrows in (A). The Green's Functions are computed by using unit slip on the subfault where the rupture on F2 was initiated, as shown in Figure 10B by the small white rectangle along with the slip model on fault segment F2. The rupture on this fault is divided into columns with corresponding synthetics presented in Figures 10C, 10D, and 10E. (C) Lower left shows the entire waveform fit at station LSZ, synthetic is decomposed into the contribution of fault segments F1, F2, and F3 as displayed on upper left. The panel on the right panel shows the contribution of columns C-1 to C2 on F2. Figures 10D and 10E are similar as Figure 10C for stations KIEV and TAU.
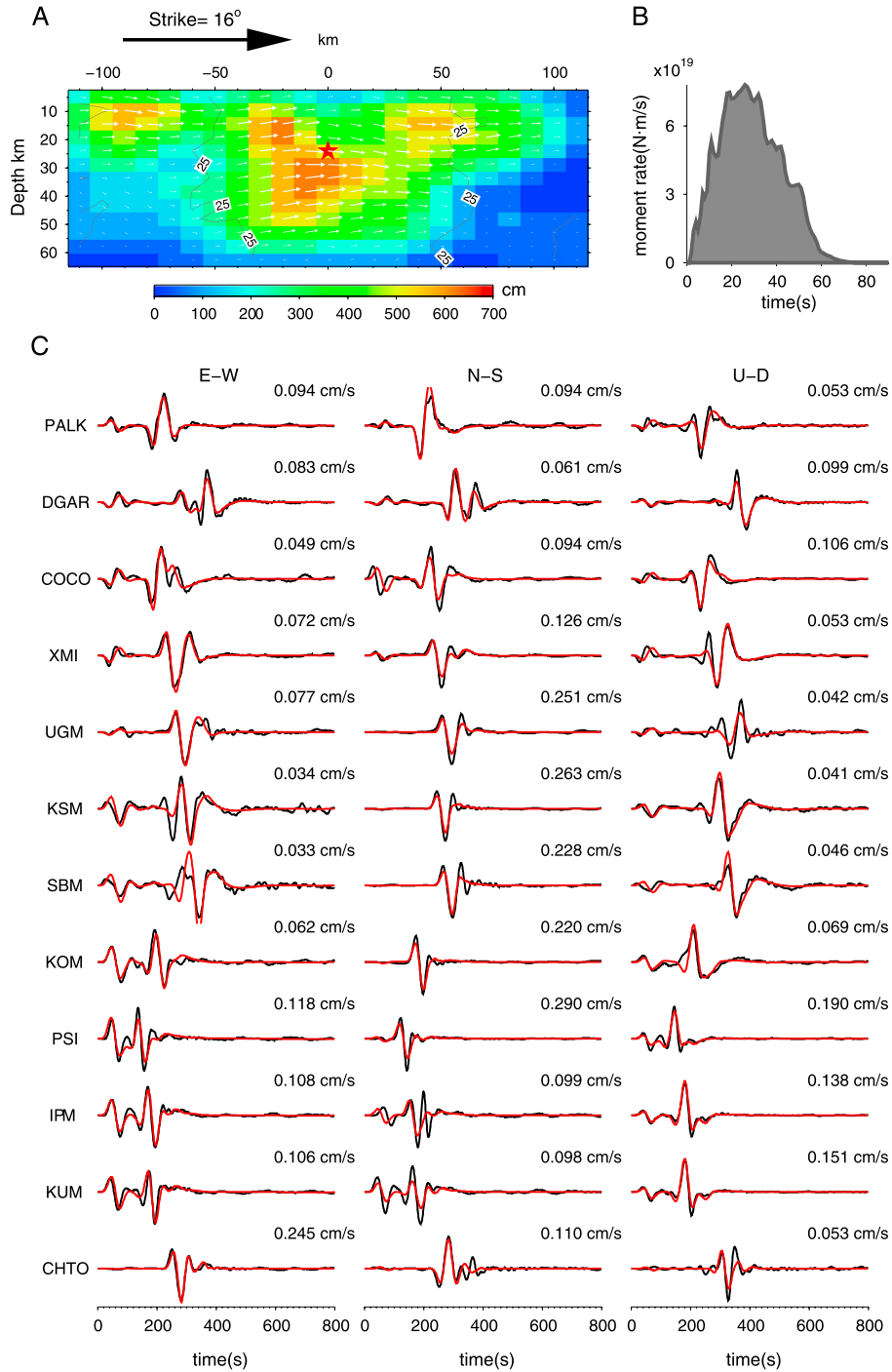
Figure 11. Slip model of M$_w$8.2 aftershock and the regional modeling. (a) The depth profile of the slip model for the M$_w$8.2 aftershock is displayed with contour lines indicating the rupture start times and the arrows show the rake angles. (b) Moment rate function. (c) Regional waveform fits with data in black and synthetics in red where all the seismograms are filtered to 50 s and longer; see Figure 8 for more detailed description.

was used to predict 10 representative teleseismic *P* waves (Figure S9), shown with the fits from the teleseismic-only inversion. Note that the prediction from the regional inversion only captures the major characteristics of the teleseismic *P* waves and misses the detailed rupture information. This is understandable because the period used is quite long (>50 s) compared with the detail of the oscillations in the

teleseismic data. The sensitivity difference between regional and teleseismic data also accounts for a large portion of discrepancy in the waveform misfit. Hence a joint inversion of both data sets is required in order to elucidate the rupture process in greater detail. We wish to re-emphasize this feature of teleseismic waveform modeling: that they are mainly controlled by the vertical velocity structure in the

source region, which is much simpler to construct in comparison with the complicated 3D lateral variations involved in modeling the regional data.

5.3. Teleseismic Waveform Sensitivity

[24] The teleseismic waveform fittings for 31 P waves and 23 SH waves are displayed in Figure 9. Most of the waveforms are well matched, and the P wave records show much more complexity than the SH waves. The discrepancies between the P and the SH waves are mainly due to the difference in their frequency contents. Thus, the complexity of the rupture process is better shown in the higher-frequency P waves. To better understand the finite-source process, we also separated the wavefield into contributions from the individual faults, similar to the approach used in the previous section. Decompositions of three representative stations are shown in Figure 10, and the separation of all stations is given in Figure S10. Because the contribution of F2 is dominant in the regional case (Figure 8 and Figure S7), we focus on more detailed separation for the F2 rupture and examine how the shallow asperity (around 10 – 40 s) and the deep asperity (~75 s) interfered to produce particular waveform characteristics. The features chosen for further examination are indicated in the boxes marked on Figure 9. Box 1 contains data from southern Africa at azimuths 236° to 268° where the radiation for the direct P wave is strong. However, the amplitude is not as strong as those shown in Box 2 at azimuths 317° to 342°. These are controlled by the directivity from the strongest patch on F2. We chose stations LSZ and KIEV to be representative and show the results of our analyses in Figure 10, where the slip patches on F2 are further separated into the contributions from the individual subfault columns displayed on the right. Summing the four columns C-1 to C2 produces a single large pulse for KIEV (D), while for LSZ (C) they are separated by 15 s, creating two pulses. Note that the pulse at station GNI (a distance of 57°) is about twice as strong as at LSZ (a distance of 66°) at comparable ranges. The Green's Functions (Figure 10A) indicate that the waveforms at these two stations are dominated by direct P waves; thus, the shape of the waveform is mainly controlled by the relative timing between these direct waves. In Box 3, at azimuths 131° to 168°, we observe an interesting late arrival at about 70 s. This is produced by the deep asperity as demonstrated for station TAU, which is controlled by the depth phase sP (Figure 10A). This asperity generates a recognizable pulse at many azimuths but changes in shape and relative timing as the direct P and depth phases interfere, as indicated in Figure 10E. These small-scale features are less obvious in the longer period SH waveforms, although stations WB2, MANU, COEN, and PATS at azimuths toward Australia (Figure S10) are extra broad because the F1 contribution arrives earlier than that from F2 by about 20 s. In contrast, they arrive together toward the north, e.g., station TLY, making a shorter and stronger pulse. In short, the directivity seen in the P waveforms is supported by these SH waveforms but because the rupture velocity is relatively low (about 2 – 2.5 km/s), these features are not as obvious as for some other events, e.g., the 2002 Denali, Alaska event, [*Ji et al*., 2004] where the rupture velocity was over 3 km/s and was unilateral.

5.4. Modeling of the M_w8.2 Aftershock

[25] We have presented an analysis of seismic data for the main (M_w8.6) Sumatra event involving a combination of regional (horizontal paths) and teleseismic (vertical paths) data. Both data sets require strong deep patches of substantial slip offsets, which if occurring separately, would be >M_w8.0 events. Such deep strike-slip source excitation has not been detected to date. Validating these results has proved to be difficult because of the lack of static data or other direct measurements. However, an M_w8.2 aftershock occurred about 2 h after the main shock, with its epicenter located near the deep slip patches on F2 (Figure 1B), which provides further evidence of deep rupture. However, it is difficult to isolate the record of this aftershock from the long-period noise of the main shock at teleseismic distances. We therefore focused on using regional data to examine its rupture characteristics with the finite-fault inversion results displayed in Figure 11. The result of each iteration in the simulated annealing inversion process is shown in Anim. S2 (see supplement). The inversion provided a well-behaved solution that again involved a large slip at depth (up to 50 km). The horizontal dimension of the slip model (about 150 km) is consistent with the aftershock distribution (Figure 1B) and the back projection results. The 150 km along-strike fault dimension and the relatively short duration (~60 s) demand a deep rupture to match the large moment magnitude of this aftershock. Together with another deep aftershock (46 km deep, Figure 5), as reported in previous sections, we consider that this earthquake sequence ruptured the entire lithosphere with an almost complete stress drop, which is discussed further in the next section.

6. Discussion

[26] We were able to derive source models for the M_w8.6 main shock and the M_w8.2 aftershock from the 2012 Wharton Basin earthquake sequence. These models are to first-order consistent with the complex geometry and time history of the ruptures derived from back projection of the high-frequency teleseismic record and from the modeling of long period (T >200 s) records of the W-phases [*Duputel et al*., 2012; *Meng et al*., 2012]. This study confirms that these earthquakes ruptured a complex set of strike-slip faults intersecting at a relatively high angle.

6.1. Stress Drop and Rupture Speed

[27] A 3D view of the bathymetry and source models of this sequence is shown in Figure 12. The rupture of the main shock started on fault F1 and propagated unilaterally westward. The rupture initiated on fault F2 at about 10 s (all times are relative to the onset of rupture on F1). It propagated bilaterally, initially rupturing a major asperity between 15 s and 45 s, with up to 24 m of slip at a depth of about 25 km, centered close to the intersection with F1. A second asperity, located about 100–150 km to the south at a depth of about 40 km, ruptured between 70 and 100 s. Still as part of the main shock, the rupture continued on F3 with two main asperities rupturing between 100 and 120 s and then between 160 and 180 s. Although the regional data provide limited resolution, it does appear that the first
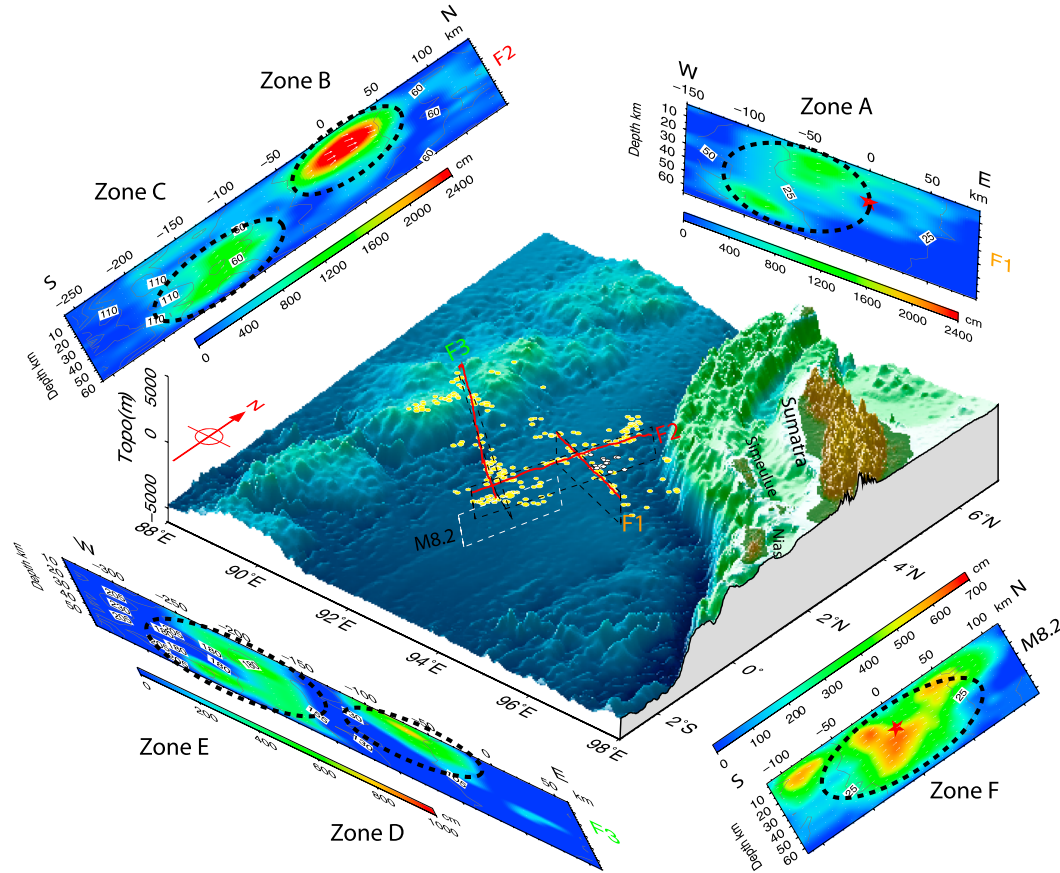
Figure 12. 3D view of the Sunda trench and fault geometry. The middle image is a 3D view of bathymetry and topography along with the schematic fault segments shown as rectangles. The red lines are the projection of the upper boundary of fault plane of F1, F2, and F3 on the seafloor. Aftershocks are shown as yellow dots, and the white dots are the foreshocks. Smoothed depth profiles of slip for the three subfaults (F1, F2, and F3), and the $M_w 8.2$ aftershock are shown along the sides.

asperity was shallow ($10 - 20$ km), while the second occurred at considerable depth ($20 - 50$ km). The $M_w 8.2$ aftershock, which happened on a fault almost parallel to F2, had relatively short source duration with slip also extending as deep as 50 km.

[28] Due to the compact slip distribution and the large slip amplitude, the estimated stress drop based on our joint inversion model ranges from 5 to 31 MPa (Table 2 and Figure 12). Here the stress drop is calculated using the formula of [*Kanamori and Anderson*, 1975] assuming rectangular asperities, which are indicated as Zones A–F in Figure 12. The largest stress drops (~30 MPa) correspond to the two asperities on fault segment F2 and are about 10 MPa for slip patches on segment F1 and F2. The high-stress drops reported here are consistent with global studies that show that intraplate earthquakes and strike-slip events on oceanic transform faults tend to have larger stress drops than other types of earthquakes, typically around 6 MPa [e.g., *Allmann and Shearer*, 2009; *Boettcher and McGuire*, 2009; *Choy and McGarr*, 2002; *Kanamori and Anderson*, 1975]. The values reported here are in the upper ends of those reported in previous studies for intraoceanic and transform fault events, probably because our analysis was carried out in greater detail (slip distributions), while methods based on the corner frequency provide only a spatial average.

[29] Our model indicates that the rupture propagated along the complex fault system with a relatively uniform rupture speed of about $2.0 - 2.5$ km/s, which is about half the shear wave speed at the depth range of the asperities. This is consistent with the results obtained from other teleseismic inversion [*Yue et al.*, 2012] and back projection studies of high-frequency waveforms, which indicate an almost constant rupture speed of 2.5 km/s [*Meng et al.*, 2012]. The main aftershock, the $M_w 8.2$ earthquake that occurred 2 h after the main shock, has characteristics similar to those of the main shock. It ruptured a few large stress drop asperities spanning a depth range of $10 - 50$ km, with a similar rupture velocity of about 2 – 2.5 km/s. The rupture velocity derived in this study is also consistent with those derived from intraoceanic and oceanic transform events [e.g., *Abercrombie and Ekstrom*, 2001]. The highly dissipative and slow rupture inferred from previous studies of such events [*Ihmlé and Jordan*, 1994; *McGuire et al.*, 1996] thus might hold only for smaller shallow events for which

Table 2. Stress Drop for Major Asperities of the Main Shock and $M_w 8.2$ Aftershock

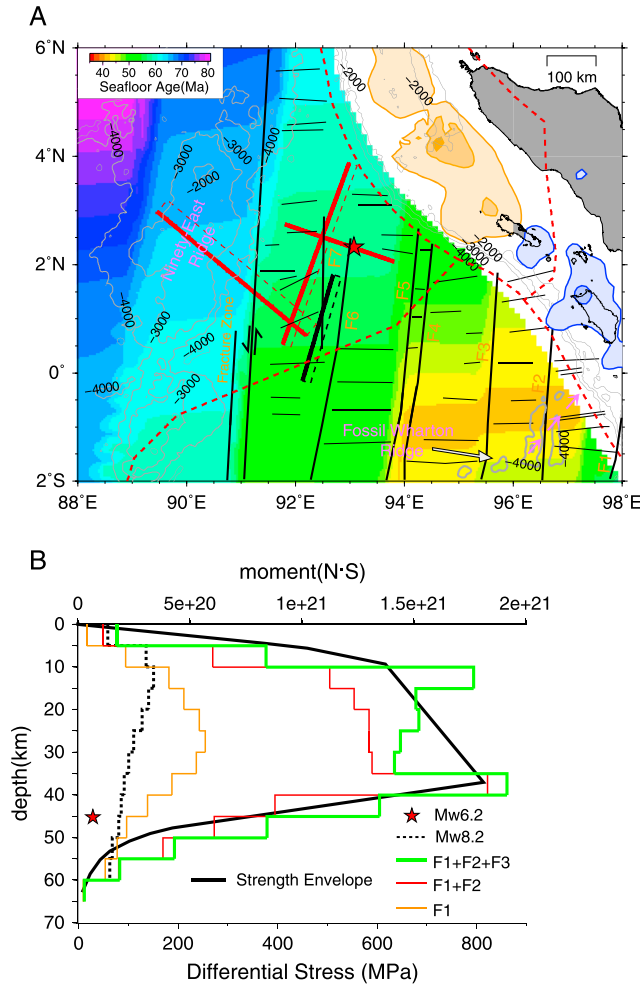| Zone	A	B	C	D	E	F
Averaged Stress Drop (MPa)	14.0	27.0	31.0	10.0	5.0	7.0

Figure 13. Fracture zone, seafloor age, and the moment depth distribution. (a) Fracture zones (denoted as black lines and marked as F1 to F7) in this region are overlapping with the seafloor ages [*Muller et al.*, 2008]. The red rectangles are the map view of the three fault planes used in the inversion, and the red star is the epicenter of the main event; the black rectangle is the fault plane for the $M_w8.2$ aftershock. Note that the Fossil Wharton Ridge is subducting beneath the Sunda trench. Slip models of the 2004 ($M_w9.2$, yellow) and 2005 ($M_w8.6$, blue) megathrusts are shown as contours. The red dashed lines are the plate boundaries from *Bird* [2003]. (b) Depth distribution of moment release for both the main shock and the $M_w8.2$ aftershock; the contribution from different segments to the main shock is shown in different colors. The point source location of the $M_w6.2$ is indicated by the red star. The black solid line is the strength envelope of the oceanic lithosphere, which is computed by the Byerlee's frictional sliding rule for the dry rock and rheology for olivine for the plastic flow [*Kohlstedt et al.*, 1995].

the nucleation phase might represent a larger fraction of the total rupture. It could also be a result of plate history, dependent upon the unique tectonic structure for this particular region.

6.2. Lithospheric Strength and Tectonic Implications

[30] The age of the Wharton Basin is estimated to be between 45 and 65 Ma [*Muller et al.*, 2008] (Figure 13A).

There are no direct constraints on the thickness of the lithosphere here, but global and regional studies show that an oceanic lithosphere of this age is typically about 60 km thick [*Gaherty et al.*, 1996; *Priestley and McKenzie*, 2006; *Tan and Helmberger*, 2007]. Thus, it appears that this exceptional earthquake ruptured the entire lithosphere along several fractures. Although direct measurements of oceanic lithospheric thickness are not available for this region, experimental and theoretical studies can provide some estimates of strength. In Figure 13B, we show the strength envelope of the oceanic lithosphere along with the depth distribution of the moment for both the main shock and the aftershocks. Here the lithospheric strength is calculated by combining Byerlee's frictional sliding rule, with friction coefficient of 0.6, for dry rock at shallow depth and the rheology for olivine for the plastic portion [*Kohlstedt et al.*, 1995]. A geotherm for a 60 million year old lithosphere and a strain rate of 10^{-15}/s is assumed. The consistent between the strength envelope and the depth consistency of released moment suggests that the earthquake sequence ruptured through the entire lithosphere.

[31] In contrast to the high friction coefficient (0.6) as used for calculating the strength envelope, *Meng et al.* [2012] consider a pressure-insensitive strength of the deep oceanic lithosphere and rather small friction coefficient (less than 0.2) to explain the almost perpendicular rupture faults and the rupture branching obtained by back projection results. This is inconsistent with the study by *Choy and McGarr* [2002] in which large stress drops (5–25 MPa) were found for some of the intraplate earthquakes and interpreted with strong oceanic lithosphere. The large stress drop as reported in our study is more consistent with the latter explanation except that in this case the earthquake ruptured the entire
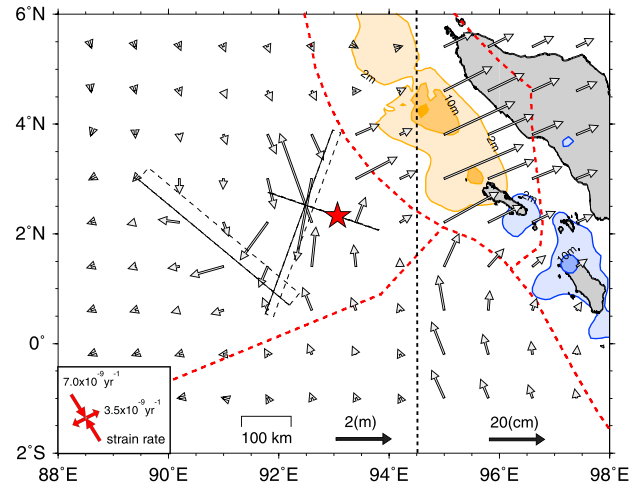

Figure 14. Prediction of static horizontal motion. The horizontal motion (vectors) predicted by the preferred slip model. Note the scale is different by a factor of 10 for the region to the east and west of 94.5°E longitude line (dashed). The 2004 and 2005 megathrusts are shown as color contours. The red dashed lines are the plate boundaries. The fault planes used in the inversion are shown as rectangles. Note that the region has undergone a net compression as indicated by the arrows. The red arrows in the lower left corner indicate the strain rate in this region based on the model presented by [*Delescluse and Chamot-Rooke*, 2007].

lithosphere. This interpretation, although a real possibility, remains puzzling since the tectonic community has little experience with this type of earthquake sequence. Generally, the well-studied events along large know strike-slip faults, i.e., along the San Andreas Fault in California, have generated little evidence for deep ruptures [*Wald et al.*, 1993]. It appears that this is largely because of weak lithosphere, or thin upper mantle lid, beneath the plate boundaries. This subject is addressed in *Melbourne and Helmberger* [2001] which summarizes the mapping of the strong Pacific upper plate structure juxtaposition with the weaker basin-and-range continental North America. A fast lid layer along the Southern California coast has a thickness over 50 km which reduces to less than 5 km approaching the San Andreas Fault. This structure agrees with the dextral strain patterns of GPS which suggests that this lid feature impacts the deformation. With no lid, it is not likely that a San Andreas event would rupture the mantle. Thus, the deep rupture and associated high-stress drop suggests a strong lithosphere which ruptured entirely during the 2012 earthquake sequences.

[32] Whole-lithosphere failure is also consistent with previous studies that show the Wharton Basin as part of a diffuse zone of active deformation separating the Australian from the Indian Plate [*Delescluse and Chamot-Rooke*, 2007; *Deplus et al.*, 1998] (Figures 1 and 14). Recent marine geophysical investigations in that area have found evidence for active deformation on north-south trending faults, probably resulting from the reactivation of the tectonic fabric of the seafloor [*Singh et al.*, 2011]. We note that our fault F2 is close to, and subparallel with, some transform faults with some well-developed fracture zones running NNE intersecting the Sunda Trench (Figure 13), namely fracture zones F6 and F7. These fracture zones have been observed to extend below the Moho of the oceanic crust and to cut through its sediment cover [*Singh et al.*, 2008]. Rupture on F2 of the main shock and the M_w8.2 aftershock have probably reactivated this fracture zones.

[33] The coseismic deformation produced by this event might help us to understand the cause of its formation. In Figure 14, we present the static surface displacements predicted from our slip model. The large-scale pattern of horizontal displacements (left-hand side of Figure 14) indicates compression in the NNW-SSE direction and extension in the ENE-WSW direction, bounded by these left-lateral strike-slip faults, which is consistent with the strain-rate modeling results (lower left, red arrows) in this region [*Delescluse and Chamot-Rooke*, 2007]. The incremental strain produced by this earthquake sequence is thus consistent with the regional strain of the deformation zone separating the Australian and Indian plates.

[34] Our results indicate that this earthquake sequence has reloaded the main asperity around the epicentral area of the 2004 Sumatra earthquake. This suggests that the Wharton Basin sequence may have been triggered by unclamping in response to the 2004 event (the effect of the M_w8.6 2005 Nias-Simeulue earthquake is negligible in comparison for that area). Also, it should be noted that the earthquake sequence lies close to the outer rise of the subducting plates. Interplay between outer rise events and megathrust earthquakes has been reported in a number of previous studies [e.g., *Dmowska and Lovison*, 1992]. The difference here is that, rather than outer rise normal events, the Sumatran

earthquake triggered a set of strike-slip events, because of the strike-slip tectonic regime that results from the diffuse zone of deformation separating the Australian and Indian plates. Note that it will be possible to test the surface displacements predicted by our model using the geodetic measurements obtained from the Sumatran GPS Array.

7. Conclusions

[35] We were able to produce a finite-source model of the Wharton Basin earthquake sequence by combined modeling using both the teleseismic and regional seismic records, and taking into account constraints on fault geometry provided by back projection studies and aftershocks. We were successful in using the regional waveforms because of the calibration derived from the M_w7.2 foreshock and the M_w6.2 aftershock. The results of our study can be summarized as follows:

[36] 1. The main shock ruptured at least three fault segments (F1, F2, and F3). The rupture delay between F1 and F2 was 10 s, and the delay was 80 s for the rupture between F1 and F3. The total moment of the earthquake was 1.3×10^{22} N·m, and the total duration was about 200 s. The moment distributions on F1, F2, and F3 were 3.3×10^{21} N·m, 8.0×10^{21} N·m, and 1.9×10^{21} N·m, respectively.

[37] 2. Both the main shock and the M_w8.2 aftershock show slip patches as deep as 50 km. The largest coseismic slip for the main event is up to 24 m and is located on F2 near the intersection of F1 and F2. The estimated stress drop ranges from 5 to 31 MPa for the main shock and is about 7 MPa for the M_w8.2 aftershock.

[38] 3. This earthquake sequence has reactivated the NNE-SSW oriented fracture zones in the Wharton Basin and some ENE-WSW oriented faults, including a segment cutting across the Ninety-East Ridge.

[39] 4. This earthquake sequence is part of the diffuse deformation zone between the Indian and Australian plates.

[40] 5. This earthquake sequence was probably triggered by static stress change induced by the M_w9.2 great Sumatra earthquake of 2004.

References

Abercrombie, R. E., and G. Ekstrom (2001), Earthquake slip on oceanic transform faults, *Nature*, *410*(6824), 74–77.

Allmann, B. P., and P. M. Shearer (2009), Global variations of stress drop for moderate to large earthquakes, *J. Geophys. Res.*, *114*, B01310, doi:10.1029/2008jb005821.

Ammon, C. J., et al. (2005), Rupture process of the 2004 Sumatra-Andaman earthquake, *Science*, *308*(5725), 1133–1139.

Bassin, C., G. Laske, and G. Masters (2000), The current limits of resolution for surface wave tomography in North America, *Eos. Trans. AGU*, 81(48), Fall Meet. Suppl., Abstract S12A-03.

Bird, P. (2003), An updated digital model of plate boundaries, *Geochem. Geophys. Geosyst.*, *4*(3), 1027, doi:10.1029/2001gc000252.

Boettcher, M. S., and J. J. McGuire (2009), Scaling relations for seismic cycles on mid-ocean ridge transform faults, *Geophys. Res. Lett.*, *36*, L21301, doi:10.1029/2009gl040115.

Choy, G. L., and A. McGarr (2002), Strike-slip earthquakes in the oceanic lithosphere: observations of exceptionally high apparent stress, *Geophys. J. Int.*, *150*(2), 506–523.

Chu, R. S., S. J. Wei, D. V. Helmberger, Z. W. Zhan, L. P. Zhu, and H. Kanamori (2011), Initiation of the great M(w) 9.0 Tohoku-Oki earthquake, *Earth Planet. Sci. Lett.*, *308*(3-4), 277–283.

Delescluse, M., and N. Chamot-Rooke (2007), Instantaneous deformation and kinematics of the India-Australia Plate, *Geophys. J. Int.*, *168*(2), 818–842.

Deplus, C., M. Diament, H. Hebert, G. Bertrand, S. Dominguez, J. Dubois, J. Malod, P. Patriat, B. Pontoise, and J. Sibilla (1998), Direct evidence of active deformation in the eastern Indian oceanic plate, *Geology*, *26*, 131–134.

Dmowska, R., and L. C. Lovison (1992), Influence of Asperities Along Subduction Interfaces on the Stressing and Seismicity of Adjacent Areas, *Tectonophysics*, *211*(1-4), 23–43.

Duputel, Z., H. Kanamori, V. C. Tsai, L. Rivera, L. S. Meng, J. P. Ampuero, and J. Stock (2012), The 2012 Sumatra great earthquake sequence, *Earth Planet. Sci. Lett.*, *351–352*, 247–257.

Gaherty, J. B., T. H. Jordan, and L. S. Gee (1996), Seismic structure of the upper mantle in a central Pacific corridor, *J. Geophys. Res.*, *101*(B10), 22,291–22,309.

Ihmlé, P. F., and T. H. Jordan (1994), Teleseismic search for slow precursors to large earthquakes, *Science*, *266*(5190), 1547–1551.

Ishii, M., E. Kiser, and E. L. Geist (2013), M-w 8.6 Sumatran earthquake of 11 April 2012: Rare seaward expression of oblique subduction, *Geology*, *41*(3), 319–322.

Ji, C., D. J. Wald, and D. V. Helmberger (2002a), Source description of the 1999 Hector Mine, California, earthquake, part I: Wavelet domain inversion theory and resolution analysis, *Bull. Seismol. Soc. Am.*, *92*(4), 1192–1207.

Ji, C., D. J. Wald, and D. V. Helmberger (2002b), Source description of the 1999 Hector Mine, California, earthquake, part II: Complexity of slip history, *Bull. Seismol. Soc. Am.*, *92*(4), 1208–1226.

Ji, C., D. V. Helmberger, and D. J. Wald (2004), A teleseismic study of the 2002 Denali fault, Alaska, earthquake and implications for rapid strong-motion estimation, *Earthq. Spectra*, *20*(3), 617–637.

Kanamori, H., and D. L. Anderson (1975), Theoritical basis of some empirical relations in seismology, *Bull. Seismol. Soc. Am.*, *65*, 1073–1095.

Kohlstedt, D. L., B. Evans, and S. J. Mackwell (1995), Strength of the Lithosphere - Constraints Imposed by Laboratory Experiments, *J. Geophys. Res.*, *100*(B9), 17,587–17,602.

Konca, A. O., V. Hjorleifsdottir, T. R. A. Song, J. P. Avouac, D. V. Helmberger, C. Ji, K. Sieh, R. Briggs, and A. Meltzner (2007), Rupture kinematics of the 2005 M-w 8.6 Nias-Simeulue earthquake from the joint inversion of seismic and geodetic data, *Bull. Seismol. Soc. Am.*, *97*(1), S307–S322.

Kustowski, B., G. Ekstrom, and A. M. Dziewonski (2008), Anisotropic shear-wave velocity structure of the Earth's mantle: A global model, *J. Geophys. Res.*, *113*, B06306, doi:10.1029/2007JB005169.

McGuire, J. J., P. F. Ihmlé, and T. H. Jordan (1996), Time-Domain Observations of a Slow Precursor to the 1994 Romanche Transform Earthquake, *Science*, *274*(5284), 82–85.

Melbourne, T., and D. Helmberger (2001), Mantle control of plate boundary deformation, *Geophys. Res. Lett.*, *28*(20), 4003–4006.

Meng, L., J. P. Ampuero, J. Stock, Z. Duputel, Y. Luo, and V. C. Tsai (2012), Earthquake in a Maze: Compressional Rupture Branching During the 2012 M-w 8.6 Sumatra Earthquake, *Science*, *337*(6095), 724–726.

Muller, R. D., M. Sdrolias, C. Gaina, and W. R. Roest (2008), Age, spreading rates, and spreading asymmetry of the world's ocean crust, *Geochem. Geophys. Geosyst.*, *9*, Q04006, doi:10.1029/2007gc001743.

Priestley, K., and D. McKenzie (2006), The thermal structure of the lithosphere from shear wave velocities, *Earth Planet. Sci. Lett.*, *244*(1-2), 285–301.

Satriano, C., E. Kiraly, P. Bernard, and J. P. Vilotte (2012), The 2012 Mw 8.6 Sumatra earthquake: Evidence of westward sequential seismic ruptures associated to the reactivation of a N-S ocean fabric, *Geophys. Res. Lett.*, *39*, L15302, doi:10.1029/2012gl052387.

Singh, S. C., et al. (2008), Seismic evidence for broken oceanic crust in the 2004 Sumatra earthquake epicentral region, *Nat. Geosci.*, *1*(11), 777–781.

Singh, S. C., H. Carton, A. S. Chauhan, S. Androvandi, A. Davaille, J. Dyment, M. Cannat, and N. D. Hananto (2011), Extremely thin crust in the Indian Ocean possibly resulting from Plume-Ridge Interaction, *Geophys. J. Int.*, *184*(1), 29–42.

Tan, Y., and D. V. Helmberger (2007), Trans-Pacific upper mantle shear velocity structure, *J. Geophys. Res.*, *112*, B08301, doi:10.1029/2006JB004853.

Tromp, J., et al. (2010), Near real-time simulations of global CMT earthquakes, *Geophys. J. Int.*, *183*(1), 381–389.

Wald, D. J., H. Kanamori, D. V. Helmberger, and T. H. Heaton (1993), Source Study of the 1906 San-Francisco Earthquake, *Bull. Seismol. Soc. Am.*, *83*(4), 981–1019.

Wei, S. J., et al. (2011), Superficial simplicity of the 2010 El Mayor-Cucapah earthquake of Baja California in Mexico, *Nat. Geosci.*, *4*(9), 615–618.

Wei, S. J., Z. W. Zhan, Y. Tan, S. D. Ni, and D. Helmberger (2012), Locating earthquakes with surface waves and centroid moment tensor estimation, *J. Geophys. Res.*, *117*, B04309, doi:10.1029/2011jb008501.

Yue, H., T. Lay, and K. D. Koper (2012), En echelon and orthogonal fault ruptures of the 11 April 2012 great intraplate earthquakes, *Nature*, *490*(7419), 245–249.

Zhao, L. S., and D. V. Helmberger (1994), Source Estimation from Broad-Band Regional Seismograms, *Bull. Seismol. Soc. Am.*, *84*(1), 91–104.

Zhu, L. P., and D. V. Helmberger (1996), Advancement in source estimation techniques using broadband regional seismograms, *Bull. Seismol. Soc. Am.*, *86*(5), 1634–1641.

Zhu, L. P., and L. A. Rivera (2002), A note on the dynamic and static displacements from a point source in multilayered media, *Geophys. J. Int.*, *148*(3), 619–627.